hv **photonics**

Article

An Interlayer of Ultrasmall N-Rich Carbon Dots for Optimization of SnO$_2$/CsFAPbI$_3$ Interface

Igor V. Margaryan [1] , **Anna A. Vedernikova** [1] , **Peter S. Parfenov** [1] , **Mikhail A. Baranov** [1] , **Denis V. Danilov** [2] , **Aleksandra V. Koroleva** [2] , **Evgeniy V. Zhizhin** [2] , **Sergey A. Cherevkov** [1] , **Xiaoyu Zhang** [3] , **Elena V. Ushakova** [1] and **Aleksandr P. Litvin** [3],*

1   PhysNano Department, ITMO University, 49 Kronversky Ave., 197101 Saint-Petersburg, Russia
2   Research Park, Saint Petersburg State University, 199034 Saint-Petersburg, Russia
3   Key Laboratory of Automobile Materials MOE, School of Material Science & Engineering, Jilin University, Changchun 130012, China
*   Correspondence: litvin@jlu.edu.cn

Abstract: Photovoltaic devices based on organic–inorganic hybrid perovskites have engaged tremendous attention due to the enormous increase in power conversion efficiency (PCE). However, defect states formed at grain boundaries and interfaces hinder the achievement of PCE. A prospective strategy to both reduce interfacial defects and control perovskite growth is the passivation of interfaces. The passivation of the electron-transporting layer/perovskite interface with ultrasmall carbon dots (CDs) with suitable chemical composition and functional groups on their surface may simultaneously affect the morphology of a perovskite layer, facilitate charge carriers extraction, and suppress interfacial recombination. Here, we show that CDs synthesized from diamine precursors may be used as an interlayer at the SnO$_2$/FACsPbI$_3$ interface. Ultrasmall CDs form a smooth, thin layer, providing better perovskite layer morphology. CD interlayers result in an increased average perovskite grain size, suppress the formation of small grains, and improve charge carriers' extraction. As a result, photovoltaic devices with CD interlayers demonstrate a higher PCE due to the increased short-circuit current density and fill factor. These findings provide further insight into the construction of interfaces based on carbon nanomaterials.

Keywords: perovskite solar cells; carbon dots; photoluminescence; morphology

1. Introduction

Renewable energy technologies have been experiencing a burst of growth and increasing adoption across the world. Along with environmental friendliness, renewable energy is also becoming cost-competitive with fossil fuels. Solar energy has significantly reduced in cost over the past decade, becoming more economically affordable [1–3]. However, there are still challenges to its widespread adoption. Despite a high PCE, the most commonly used silicon solar cells have some drawbacks. Although their cost has decreased considerably, they are still relatively expensive. Moreover, requiring much energy and high temperatures, the production of silicon wafers leads to the generation of a large amount of waste [4,5]. For these reasons, metal-halide perovskites have become one of the most promising materials for application in low-cost and easy-to-fabricate photovoltaics of the next generation.

Metal-halide perovskites with a general structural formula ABX$_3$ (where A stands for monovalent cation (methylammonium (MA), formamidinium (FA), Cs), B stands for metal divalent cation (Pb, Sn, Ge, etc.), and X stands for halide anion (Cl, Br, I)) have recently appeared as a rising star in the field of material science. A number of exceptional properties are well accompanied by facile synthetic approaches, allowing metal-halide perovskites to be used in numerous applications, including but not limited to photovoltaics [6,7], light emission and lasing [8–11], photocatalysis [12–15], nanophotonics [16], nonlinear-

optics [17–20], photodetection [21,22], etc. In particular, organic–inorganic hybrid perovskite solar cells (PSCs) draw tremendous attention as their power conversion efficiency (PCE) has increased from 3.8% to 25.6% since 2009 [23,24]. This incredible progress became possible due to outstanding properties of perovskites such as high charge carriers mobility [25,26], a large diffusion length [27,28], and a high absorption coefficient [29,30]. Typically, the light-absorbing perovskite active layer is sandwiched between electron- and hole-transporting layers in either mesoporous or planar PSC architectures. An adjustment of the device energy diagram allows the realization of efficient separation and transfer of photoexcited charge carriers.

Currently, organic–inorganic $MAPbI_3$ and $FAPbI_3$ hybrid perovskites are most widely used for photovoltaics. $MAPbI_3$ is more commonly used because of its higher stability. Nevertheless, $FAPbI_3$ is more optimal for photovoltaic applications due to its narrower band gap [31–34], which is beneficial for effective light absorption. However, $FAPbI_3$ suffers from poor stability, which is expressed by the spontaneous transition from black α-phase to yellow δ-phase degrading its light-harvesting ability [35–37]. A popular and effective way to tackle the stabilizing issue is the partial substitution of the FA cation with small ions, such as Cs [38–40]. For instance, it was shown that the most beneficial Cs:FA ratio in $FA_{1-x}Cs_xPbI_3$ mixed perovskite polycrystalline films may lie in the range x = 0.03–0.10 [41–43]. Under these conditions, mixed-cation chemical composition allows better morphological and optical properties of the perovskite layer, which in turn provides higher photovoltaic performance of perovskite solar cells. Furthermore, photo- and moisture-stability may be significantly improved. However, an excess of Cs may induce the undesired emergence of the $CsPbI_3$ subphase and increase of a bandgap. [7] Even so, Pb and I dangling bonds at perovskite grain boundaries and defects at the interface between the electron transport layer (ETL) and $FACsPbI_3$ active layer create trap states acting as recombination centers, hindering charge extraction and lowering PCE. To this end, various additive engineering techniques are employed to passivate the traps in the perovskite active layer or at the ETL/perovskite interface. Recently, carbon dots (CDs) as emerging carbon nanoparticles with unique optical parameters [44,45] have been studied as a promising candidate for defect passivation in PSCs. Carbon dots are environmentally friendly and low-cost particles, which make them desirable for use in PSCs [46–48]. They can also be used as interlayers between ETL and perovskite incorporated into a perovskite layer [49–51]. Moreover, CDs are reported to improve the perovskite layer morphology resulting in larger grains and fewer trap sites at its boundaries [52–55].

Herein, we have studied the properties of 2 types of CDs, namely CD_E synthesized from ethylenediamine (EDA) and CD_{EO} synthesized from O-phenylenediamine (o-PD) and EDA. We employed CD_E and CD_{EO} as interlayers between SnO_2 ETL and $FACsPbI_3$ active layer and determined their influence on the optical and morphological properties of the perovskite thin film. We revealed that such CD interlayers facilitate better perovskite morphology and more efficient charge carrier extractions. As a result, CD interlayers improve the operational characteristics of perovskite-based photovoltaic devices.

2. Materials and Methods

Formamidinium iodide (FAI, $\geq$98%), lead(II) iodide (PbI_2, $\geq$99.99%), Cesium iodide (CsI, $\geq$99.99%), N,N-Dimethylformamide (DMF, $\geq$99.8%), Dimethylsulfoxide (DMSO, $\geq$99.7), Spiro-MeOTAD ($\geq$99%), Bis(trifluoromethylsulfonyl)amine lithium salt (Li-TFSI, $\geq$99.95%), 4-tert-Butylpyridine (t-Bp, $\geq$98%), Chlorobenzene (CB, $\geq$99.8%), Acetonitrile (I, anhydrous, 99.8%), 2-methoxyethanol (anhydrous, $\geq$99.8%), O-phenylenediamine (flaked, 99.5%), acetylacetone (AA, $\geq$99%), and ethylenediamine (EDA, $\geq$99.5%) were purchased from Sigma-Aldrich (Darmstadt, Germany). All reagents were of analytical grade and used directly without further purification. Deionized water was produced through a Millipore water purification system (Milli-Q, Millipore, Bedford, MA, USA) and used throughout the study.

2.1. Carbon Dots (CDs) Synthesis

CDs samples were obtained by one-step solvothermal heating of the precursor's solution. Sample CD_E was synthesized from 0.5 mL of EDA dissolved in 5 mL of acetylacetone. Sample CD_{EO} was synthesized from 0.135 g of o-PD and 0.75 mL of EDA dissolved in 5 mL of acetylacetone. The solutions were transferred into a 40 mL Teflon reactor for a solvothermal reaction at 190 °C for 8 h. After the reaction, the autoclaves were naturally cooled down to room temperature. The as-prepared CD solutions were transferred to dialyzed tubes with a molecular weight of 7000 Da for 24 h to remove unreacted precursors and molecular fluorophores.

2.2. Thin Films and Device Fabrication

The studied SnO_2/CDs and SnO_2/CDs/perovskite films were fabricated the same way as in photovoltaic devices. ITO/glass substrates were cleaned and dried by nitrogen flow and exposed to ultraviolet ozone for 20 min before SnO_2 deposition. Commercial SnO_2 colloidal solution was diluted with DI water in a 1:1 ratio and ultrasonicated for one hour. The $FA_{0.9}Cs_{0.1}PbI_3$ precursor was prepared in a glovebox according to Sanchez-Godoy et al. [56] as follows. CsI (30 mg) was completely dissolved in a DMF:DMSO (4:1) solvent mixture. Once the CsI dissolved, FAI (178.7 mg) was added and stirred until completely dissolved. Then PbI_2 (461 mg) was added and heated to 70 °C. The solution was left to stir overnight. The perovskite precursor solution was filtered using a 0.45 µL hydrophobic filter prior to use. To form a thin layer on the top of SnO_2, CDs were dried and re-dispersed in 2-methoxyethanol. To prepare the Spiro-OMeTAD precursor solution, 72.5 mg of Spiro-OMeTAD powder was dissolved in 1 mL of chlorobenzene in the glove box and left to stir overnight. Then, 17.5 µL of Li-TFSI (520 mg/mL in acetonitrile) and 28.8 µL of t-BP were added to the Spiro-OMeTAD precursor and stirred for 3 h. The Spiro-OMeTAD precursor was filtered using a 0.45 µL hydrophobic filter prior to use.

The SnO_2 precursor was spun on an ITO substrate at 2000 rpm for 5 s and at 4000 rpm for 30 s, followed by annealing at 180 °C for an hour to form ETL. Prior to the deposition of the next layer, annealed SnO_2 substrates were treated with an ultraviolet ozone for 20 min. To form SnO_2/CD_E and SnO_2/CD_{EO} layers, 50 µL of CD_E and CD_{EO} solutions were spun on the SnO_2 layer at 4000 rpm for 40 s, followed by annealing at 130 °C for 15 min. An amount of 36 µL of $FA_{0.9}Cs_{0.1}PbI_3$ perovskite precursor was spun at 1000 rpm for 10 s and 5000 rpm for 30 s. An amount of 100 µL of chlorobenzene was dripped onto the spinning substrate at the 25th second from the beginning. Thereafter, the perovskite films were annealed at 150 °C for 10 min. Once the samples cooled to room temperature, 25 µL of the Spiro-OMeTAD precursor was spin-coated at 5000 rpm for 30 s to form a hole-transporting layer. Finally, 80 nm-thick Ag electrodes were deposited by thermal evaporation.

2.3. Characterization

The absorption spectra of the solutions were obtained on a UV-3600 spectrophotometer (Shimadzu, Kyoto, Japan). The photoluminescence (PL) characteristics were studied using an FP-8200 spectrofluorometer (Jasco, Tokyo, Japan) and a purpose-built setup for PL analysis [57] for CDs colloidal solutions and perovskite films, respectively. To record FTIR spectra, a Tensor II FTIR spectrophotometer (Bruker, Ettlingen, Germany) was used. Time-resolved PL decay curves were measured using a MicroTime 100 microscope (PicoQuant, Berlin, Germany). Escalab 250Xi (Thermo Fisher Scientific, Waltham, MA, USA) was used for X-ray photoelectron spectroscopy (XPS). A Zeiss Libra 200FE (Zeiss, Oberkochen, Germany) microscope was used for transmission electron microscopy (TEM). A surface morphology study was performed by atomic force microscopy (AFM) (NT-MDT SPM–Nova, Moscow, Russia). J-V characteristics of photovoltaic cells were measured by using a Keithley 2400 source meter (Keithley Instruments, Cleveland, OH, USA) under a stimulated AM 1.5G spectrum. The mask with an area of 0.01 cm^2 was used for J-V measurements.

3. Results

CDs were produced schematically, as shown in Figure 1a,b. Different diamine precursors were used to provide a better passivation of the perovskite material through embedding in the crystal structure at the A cation site. The acetylacetone was chosen as reactive media to obtain CDs soluble in non-polar solvents. The mixture of precursors in solution was heated in a Teflon reactor solvothermal and then the product was thoroughly washed by dialysis. Figure 1c shows a typical TEM image of CD_E. It is seen that CDs are quasi-spherical nanoparticles with a size below 10 nm. Commonly, CDs are partially carbonized particles, as was shown for ethylenediamine-based CDs [58] and o-phenylenediamine-based CDs [59]. X-ray photoelectron spectroscopy (XPS) was used to determine the chemical composition of CD_E. From the full survey XPS spectrum of CDE, the CDs are composed of 67% C, 28.8% O, and 4.2% N (Figure 1d). The high-resolution XPS spectra of each element shown in Figure 1e–g demonstrate that the CDs are carbonized particles with carboxylic, hydroxylic, and amide groups at the surface.
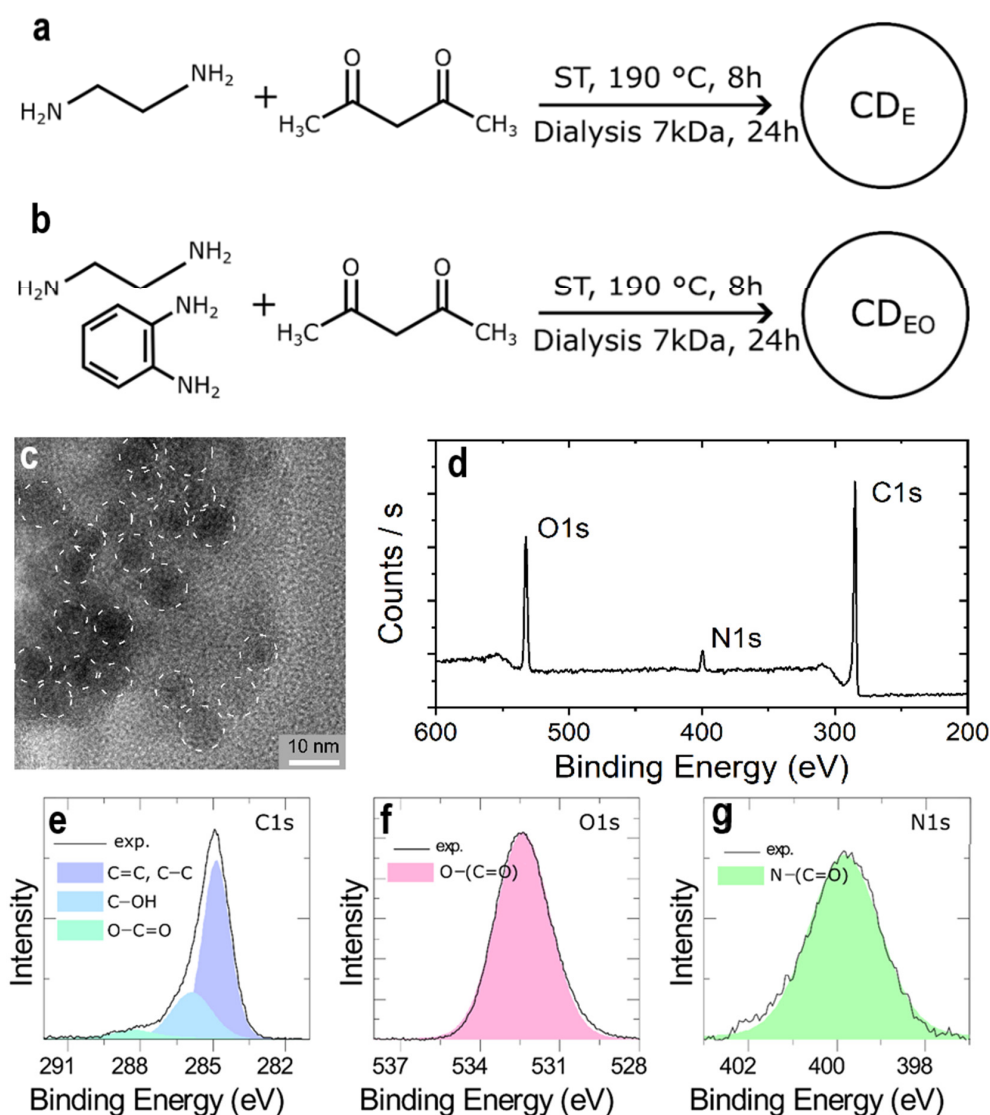
Figure 1. Schematic representation of CD_E (**a**) and CD_{EO} (**b**) synthesis. (**c**) Typical TEM image obtained for CD_E. Full survey XPS spectrum (**d**) and corresponding high-resolution XPS spectra for carbon (**e**), oxygen (**f**), and nitrogen (**g**) elements obtained for CD_E.

The absorption spectra of CDs are shown in Figure 2a. CD_E has 4 absorption bands at 215, 265, 313, and 395 nm. The addition of o-PD during synthesis results in a blue shift of peak position from 265 to 255 nm and makes it less pronounced. PL excitation-emission maps for CD_E and CD_{EO} are shown in Figure 2b,c. Sample CD_E has a PL band centered at 440 nm with maximal excitation at ~325 and 265 nm, which corresponds to peaks in the absorption spectrum. For CD_{EO}, the main PL band is centered at 400 nm with maximal excitation at ~240 nm. In addition, there are 2 more centers at 425 nm with excitation at ~340 nm and 470 nm with excitation at ~390 nm.
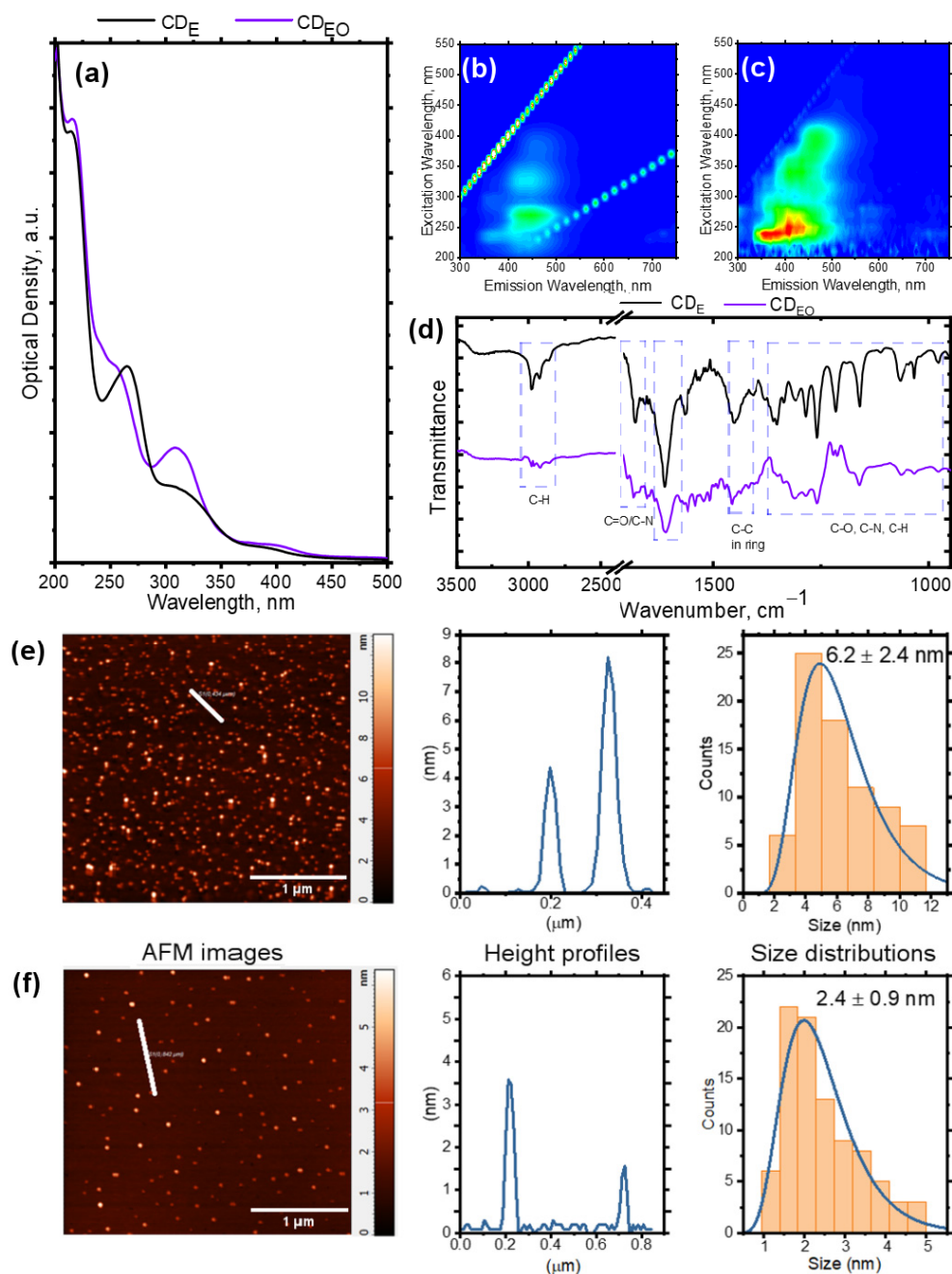
**Figure 2.** CDs characterization. (**a**) Absorption spectra of CD_E (black line) and CD_{EO} (violet line). PL excitation-emission maps for (**b**) CD_E and (**c**) CD_{EO}. (**d**) FTIR spectra of CD_E (black line) and CD_{EO} (violet line). (**e**) AFM image, height profile, and size distribution for CD_E. (**f**) AFM image, height profile, and size distribution for CD_{EO}.

FTIR spectroscopy was employed to explore the functional groups at the CD surface. The FTIR spectra of CDs are shown in Figure 2d and demonstrate peaks at 2978, 2911, and 2859 cm^{-1}, which can be attributed to C-H asymmetric and symmetric stretching. The peak at 1680 can be attributed to C=N stretching in imines and a strong peak at 1610 cm^{-1} is a product of the interaction of EDA and acetylacetone [60]. In both samples, the absorption at 1500 cm^{-1} is attributed to C=C vibrations in the aromatic ring. In the region of 1750–1450 cm^{-1}, there are typical peaks for carboxyl and amide groups, and C-H bending, and C-O, C-N stretching are observed at 1250–950 cm^{-1}. Thus, the synthesized CDs are O, N-doped nanoparticles that have molecular groups, allowing to dissolve them in both polar (as amides) and non-polar (as $-CH_x$) solvents.

The morphology of CDs was studied using AFM. Typical AFM images, height profiles, and CD size distributions are shown in Figure 2e,f. CD_{EO} has a smaller average size of 2.4 and a much narrower size distribution of 0.9 nm. To employ CD_E and CD_{EO} as axillary layers at the ETL/perovskite interface, we first studied the morphology of their thin films. Figure 3 shows (a) AFM images and (b) height profiles (aligned to the mean height values) for the SnO_2, $ITO/SnO_2/CD_E$, and $ITO/SnO_2/CD_{EO}$ films. After the deposition of CDs, the root-mean-square (RMS) roughness of the formed ETL reduces significantly. The effect is more pronounced for ultra-small CD_{EO}. Their small size and narrow size distribution allowed them to achieve the ETL with RMS as small as 0.23 nm, which facilitates the further homogeneous formation of a perovskite active layer.
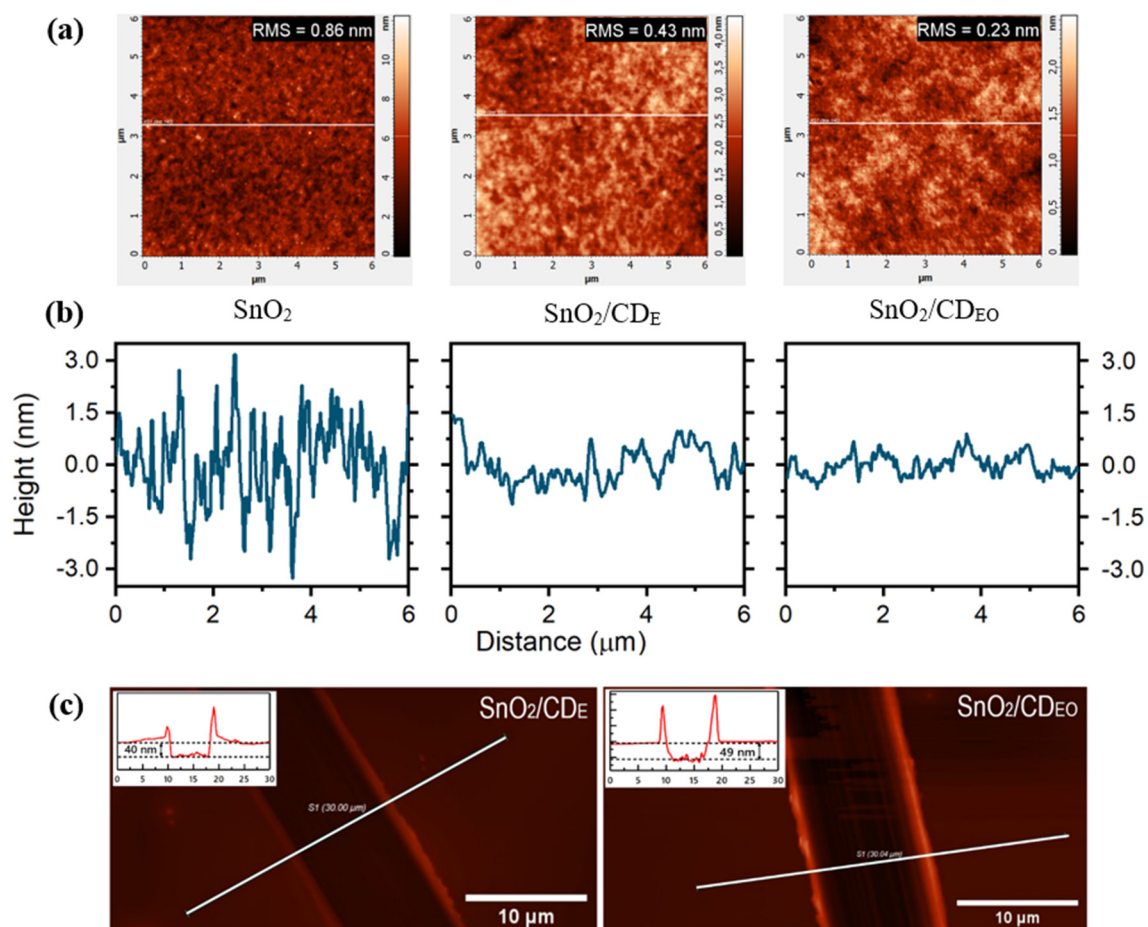
Figure 3. AFM images (**a**) and height profiles (**b**) for ITO/SnO_2, $ITO/SnO_2/CD_E$, and $ITO/SnO_2/CD_{EO}$ films. The calculated RMS of the top layers is specified in the AMF images. The thickness (**c**) of SnO_2/CD_E and SnO_2/CD_{EO} layers.

Then, the perovskite layer was deposited on pristine SnO_2 and SnO_2 covered with CD_E and CD_{EO} carbon dots. The morphology of perovskite polycrystalline films deposited on pristine SnO_2 was analyzed with SEM and AFM first. SEM analysis (Figure 4a) shows that perovskite grains have a broad size distribution. Furthermore, numerous small grains can be observed (several of them are highlighted with white circles). As a result, obtained perovskite grains sizes can be fitted with a lognormal distribution. The mean size of grains revealed with SEM is 255 ± 120 nm. Similar conclusions may be made by the analysis of corresponding AFM images (Figure 4b,c). The SnO_2/perovskite sample contains numerous grains with a quite small size of less than 200 nm as depicted with the yellow cycles in Figure 4b. An analysis of the mean size correlates with SEM data, namely, a mean size is estimated as 288 ± 196 nm. These results correlate well with those recently reported for $Cs_xFA_{1-x}PbI_3$ perovskite films formed on the SnO_2 surface [41,56].
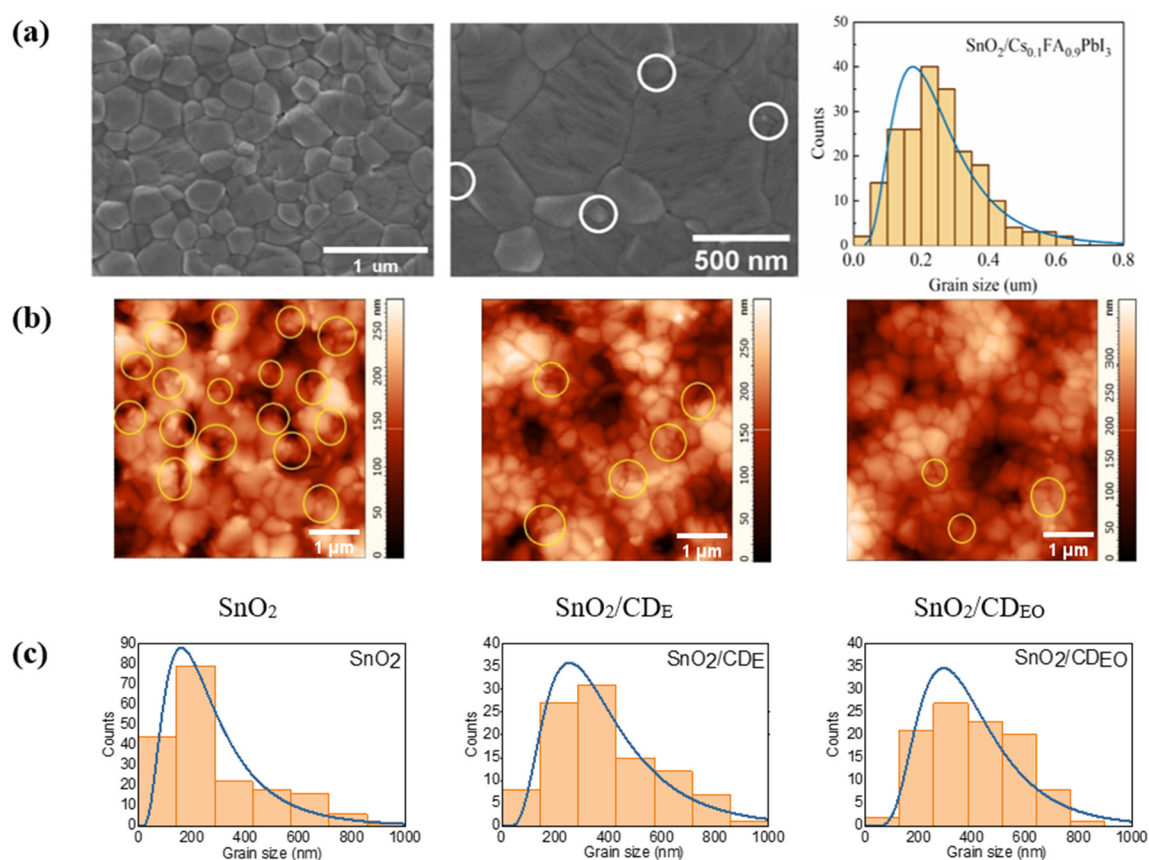
Figure 4. (**a**) SEM analysis of a polycrystalline $Cs_{0.1}FA_{0.9}PbI_3$ perovskite film formed on pristine SnO_2. AFM images (**b**) and grain size distributions (**c**) for $Cs_{0.1}FA_{0.9}PbI_3$ perovskite films formed on ITO/SnO_2, ITO/SnO_2/CD_E, and ITO/SnO_2/CD_{EO}.

Then, the morphology of the perovskite films grown on CD interlayers was studied by AFM, and a strong difference in morphologies was observed. First, an average perovskite grain size grows significantly when the film is fabricated on SnO_2 covered with CDs. Namely, an average grain size increased from 288 ± 196 nm to 391 ± 192 nm and 401 ± 166 nm when CD_E and CD_{EO} were used, respectively. Secondly, a change in grain size distribution is revealed (Figure 4b). The use of CD interlayers improves the grain size distribution. Indeed, the number of the smallest grains reduced when CD_E was used and is neglected when CD_{EO} was used. Importantly, when CD_{EO} was used as an interlayer, a perovskite film is composed of grains whose sizes are uniformly distributed in a range of $200-600$ nm.

An Increase in average grain size and suppressed formation of small-sized grains are essential for the fabrication of efficient photovoltaic devices based on polycrystalline perovskite films. As known, interfacial and trap-assisted recombination is the most detrimental source of losses limiting the performance of perovskite-based photovoltaic devices. Small average grains size or a large portion of small grains form rich grain boundaries with numerous defect states acting as centers for undesired recombination. A thin layer of CDs rich in functional groups may change a perovskite crystallization process [61]. Additionally, a smooth ETL surface formed with ultra-small CDs avoids the appearance of an excessive number of crystallization centers. A reduced number of nucleation centers may be responsible for the suppressed formation of the smallest grains which were clearly seen for the referent sample. As a result, the observed change of perovskite film morphology may play a pivotal role in the improvement of the efficiency of perovskite-based devices. The thickness of CD-modified ETLs was measured by an AFM analysis of purposely made scratches (Figure 3c). The thickness of CD_E- and CD_{EO}-modified ETLs were determined as 40 and 49 nm, respectively.

Furthermore, the impact of CD interlayers on perovskite thin film optical properties was investigated using steady-state and time-resolved (TR) PL measurements, which are commonly used methods to analyze charge carrier extraction from the active layer to charge-transport layers [62,63]. It has been recently shown that carbon nanoparticles deposited at the interfaces might serve for more efficient extraction of photoexcited charge carriers from a perovskite film, which may be revealed by employing PL spectroscopy or transient absorption measurements [64–66]. Steady-state PL (Figure 5a) demonstrates that the control sample possesses the highest PL intensity, whereas CD_E and CD_{EO} interlayers quench PL intensity by 18% and 27%, respectively. TR PL (Figure 5b) results are consistent with steady-state PL exhibiting faster PL decay when CD_E and CD_{EO} interlayers are employed. More specifically, the PL decay curves were fitted by a triple exponential decay function as follows:

$$I_{TRPL} = A_1 \cdot e^{-\frac{t}{\tau_1}} + A_2 \cdot e^{-\frac{t}{\tau_2}} + A_3 \cdot e^{-\frac{t}{\tau_3}} \tag{1}$$

where A_1, A_2, and A_3 are amplitudes and τ_1, τ_2, and τ_3 are the PL decay times of shorter, intermediate, and longer components in PL decay, respectively. The estimated values are listed in Table 1 along with an average PL lifetime calculated as follows:

$$\tau_{avg} = \frac{\sum A_i \tau_i^2}{\sum A_i \tau_i}. \tag{2}$$
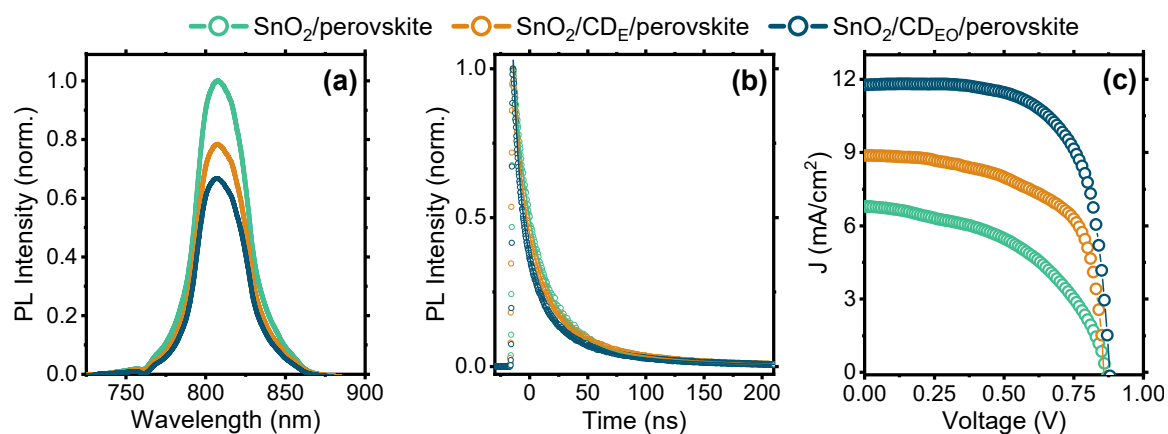
Figure 5. (**a**) Steady-state PL spectra, (**b**) PL decay curves, and (**c**) J-V curves of ITO/SnO$_2$/Perovskite, ITO/SnO$_2$/CD$_E$/Perovskite, and ITO/SnO$_2$/CD$_{EO}$/Perovskite photovoltaic devices.

Table 1. PL decay parameters for SnO_2/Perovskite, SnO_2/CD_E/Perovskite, and SnO_2/CD_{EO}/Perovskite films.

	T_{avg} (ns)	A_1	τ_1 (ns)	A_2	τ_2 (ns)	A_3	τ_3 (ns)
SnO_2/Perovskite	26.5	0.09	10.4	0.35	27.3	0.06	94.6
SnO_2/CD_E/Perovskite	21.9	0.03	6.4	0.29	22.1	0.12	75.7
SnO_2/CD_{EO}/Perovskite	20.8	0.04	5.8	0.24	21.1	0.09	82.0

The average PL decay time for the SnO_2/Perovskite control sample is 26.5 ns, whereas upon CD_E and CD_{EO} interlayers induce a decrease of τ_{avg} to 21.9 and 20.8 ns, respectively. Thus, the PL analysis reveals that CD interlayers induce PL quenching, which may be attributed to the more efficient extraction of photoexcited charge carriers from a perovskite layer, as will be further confirmed by analysis of the J-V curves obtained for corresponding photovoltaic devices. This finding is important for further improvement of perovskite-based photovoltaic devices since better charge extraction contributes to the achievement of a higher short-circuit current density (J_{SC}) value.

To investigate how the aforementioned changes in perovskite morphology and charge carrier dynamics, induced by CDs interlayers, influence the performance of perovskite-based photovoltaic devices, the devices with a structure of ITO/SnO_2(ETL)/Perovskite(Active)/Spiro-OMeTAD(HTL)/Ag were fabricated. J-V characteristics obtained for the control device and the devices with CD interlayers are shown in Figure 5c. The estimated open-circuit voltage (V_{OC}), J_{SC}, and fill factor (FF) over 16 devices of each type are shown in Figure 6, whereas averaged and champion values are listed in Table 2. It is seen that the insertion of CD interlayers allows the achievement of a higher performance of photovoltaic devices.
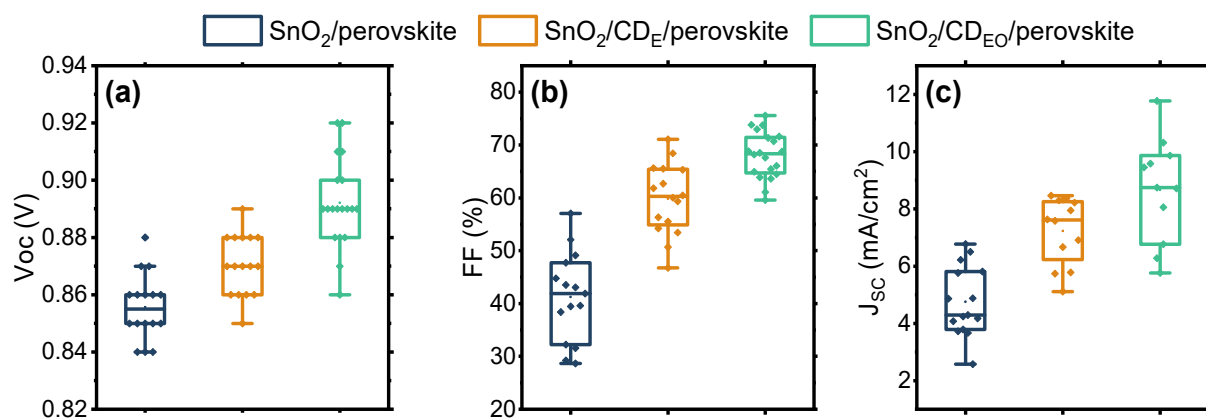
Figure 6. (**a**) J_{sc}, (**b**) V_{oc}, and (**c**) FF of control (blue) perovskite-base photovoltaic devices and the devices with CD_E (orange) and CD_{EO} (green) interlayers.

Table 2. Photovoltaic parameters (average and champion devices) of control devices, and the devices with CD_E and CD_{EO} interlayers.

Name		V_{oc} (V)	J_{sc} (mA/cm²)	FF, %	PCE, %
CD-free	Average	0.86 ± 0.01	4.8 ± 1.2	41 ± 8	1.9 ± 0.6
	Champion	0.88	6.8	57	2.9
CD_E interlayer	Average	0.87 ± 0.01	7.2 ± 1.2	60 ± 7	3.8 ± 0.5
	Champion	0.89	8.5	71	4.8
CD_{EO} interlayer	Average	0.89 ± 0.02	8.7 ± 1.8	68 ± 4	5.0 ± 1.1
	Champion	0.92	11.8	76	6.9

V_{OC} suffers minor improvement from 0.86 to 0.87 and 0.89 V when CD_E and CD_{EO} interlayers are used, respectively. In striking contrast, J_{SC} and FF grow significantly when CDs are inserted at the ETL/perovskite interface. Namely, an average J_{SC} increases from 4.8 to 7.2 to 8.7 mA/cm^2 and FF improves from 41 to 60 to 68% when CD_E and CD_{EO} were inserted at the interface. We may attribute the drastic increase in J_{SC} and FF to several factors. First, an obvious change in perovskite layer morphology (large average grain size and suppressed formation of small grains) stimulates the enhancement of both J_{SC} and FF due to reduced losses at boundary trap states. Moreover, a possible passivating effect of the CDs functional group facilitates reduced parasitic interfacial recombination, bringing higher J_{SC} and FF. Additionally, improved charge carrier extraction promotes the achievement of a higher value of J_{SC}. The improvement of these characteristics provides an increase in maximum PCE from 2.9 to 4.8 to 6.9% for the devices with CD_E and CD_{EO} interlayers, respectively. Importantly, a stronger enhancement of device performance with an interlayer formed with ultrasmall CD_{EO} is in line with the morphological and optical analysis of perovskite films.

4. Discussion

The presented experimental results evidence for an obvious influence of N-rich CDs on morphological and optical properties of a perovskite layer, as well as on the performance of the photovoltaic devices based thereof. As noted earlier, CDs modify the ETL surface in terms of its roughness, which can affect the subsequent formation of a layer of a polycrystalline perovskite film. In terms of chemical composition, CDs can have different effects both on the formation of the perovskite active layer and on the modification of the ETL properties, which leads to a change in device performance. Indeed, it was recently shown that N-doped graphene quantum dots (GQDs) influence the crystallization of MAPbI$_3$ film due to the Lewis acid-base interaction between N atoms and Pb^{2+} acid [67]. It was supposed that N-doped GQDs act as nucleation and growth centers, thus providing better and aligned perovskite morphology. More recently, Dong et al. showed that amine-rich CDs modify the crystallization of a perovskite due to a hydrogen interaction between amine groups on the CD surface and the intermediates from the perovskite solution [61]. Moreover, it was shown that nitrogen-doped CDs facilitate passivation of the surface of MAPbI$_3$ perovskites through the formation of hydrogen bonds between nitrogenous groups and undercoordinated iodine ions [53]. Furthermore, the passivation of uncoordinated Pb atoms by nitrogen atoms in N-doped CDs was also proposed [68]. The aforementioned findings, together with the presented experimental results, demonstrate the influence of CD N-doping on the formation of a perovskite active layer.

On the other hand, doping and functionalization have an invaluable effect on the optical and electrical properties of CDs. Namely, it was experimentally and theoretically shown that the electronic structure and a Fermi-level position in CDs may be tuned significantly [46]. This property is of significant importance for engineering the interfaces with the effective extraction of the photoexcited charge carriers. As an example, Zhang et al. used CDs to modify SnO$_2$ and ZnO ETLs using CDs as interlayers [51]. They demonstrated that a variation of the EDA/citric acid ratio used for the CD synthesis allows for the precise tuning of the work function of the CD-modified ITO film. Thus, amine-rich CDs were used to adjust a better energy offset between ETL and a perovskite active layer, which in turn improves the photocurrent and PCE of the corresponding photovoltaic device. Furthermore, doping and functionalization of CDs influence their conductivity. In particular, N-doping results in N-type conductivity [69], which may eventually serve for better electron transfer in photovoltaic devices. Overall, the N-functionalization of CDs has an important influence on the electrical properties of ETL in perovskite photovoltaics.

5. Conclusions

To conclude, we have demonstrated how non-toxic, low-cost, and easy-to-fabricate CDs may serve to improve perovskite-based photovoltaic devices. CDs were synthesized by a solvothermal method from different diamine precursors and acetylacetone to ensure N-rich chemical composition and solubility in non-polar solvents, respectively. We showed that CDs obtained this way may be effectively used to improve the SnO_2/perovskite interface. The modification of SnO_2 layers with ultrasmall CDs reduces the surface roughness of ETL, which in turn facilitates better morphology of a perovskite active layer. Upon CD-modification, larger average perovskite grain size and reduced formation of the smallest grain are observed. A possible influence of the N-rich chemical composition of CDs on perovskite morphology is discussed. Optical spectroscopy revealed that CD interlayers induce quenching of the perovskite PL, which was attributed to better photoexcited charge carrier extraction, in line with electrical measurements. As a result, we showed that perovskite-based photovoltaic devices with CD interlayers demonstrate better performance, mostly because of an increase in short-circuit current density and fill factor. The enhancement of device performance is attributed to improved perovskite morphology and the modification of ETL properties.

References

1. Ellabban, O.; Haitham, A.R.; Frede, B. Renewable energy resources: Current status, future prospects and their enabling technology. *Ren. Sustain. Energy Rev.* **2014**, *32*, 748–764. [CrossRef]
2. Peake, S. *Renewable Energy-Power for a Sustainable Future*; No. Ed. 4; Oxford University Press: Oxford, UK, 2018.
3. Balakrishnan, P.; Shabbir, P.S.; Siddiqi, M.F.A.; Wang, X. Current status and future prospects of renewable energy: A case study. *Energy Sources Part A Recovery Util. Environ. Effects* **2020**, *42*, 2698–2703. [CrossRef]
4. Gribov, B.G.; Zinov'Ev, K.V. Preparation of high-purity silicon for solar cells. *Inorg. Mat.* **2003**, *39*, 653–662. [CrossRef]
5. Ranjan, S.; Balaji, S.; Panella, R.A.; Ydstie, B.E. Silicon solar cell production. *Comp. Chem. Eng.* **2011**, *35*, 1439–1453. [CrossRef]
6. Xia, J.; Liang, C.; Gu, H.; Mei, S.; Li, S.; Zhang, N.; Xing, G. Surface passivation toward efficient and stable perovskite solar cells. *Energy Environ. Mat.* **2023**, *6*, e12296. [CrossRef]
7. Lee, D.K.; Park, N.G. Additive engineering for highly efficient and stable perovskite solar cells. *Appl. Phys. Rev.* **2023**, *10*, 011308. [CrossRef]
8. Kong, L.; Zhang, X.; Zhang, C.; Wang, L.; Wang, S.; Cao, F.; Yang, X. Stability of Perovskite Light-Emitting Diodes: Existing Issues and Mitigation Strategies Related to Both Material and Device Aspects. *Adv. Mater.* **2022**, *34*, 2205217. [CrossRef] [PubMed]
9. Wei, K.; Liang, B.; Sun, C.; Jiang, Y.; Yuan, M. Metal Halide Perovskites for Red-Emission Light-Emitting Diodes. *Small Struct.* **2022**, *3*, 2200063. [CrossRef]
10. Dong, H.; Zhang, C.; Liu, X.; Yao, J.; Zhao, Y.S. Materials chemistry and engineering in metal halide perovskite lasers. *Chem. Soc. Rev.* **2020**, *49*, 951–982. [CrossRef]

11. Liu, M.; Grandhi, G.K.; Matta, S.; Mokurala, K.; Litvin, A.; Russo, S.; Vivo, P. Halide perovskite nanocrystal emitters. *Adv. Photon. Res.* **2021**, *2*, 2000118. [CrossRef]

12. Cheng, P.; Han, K.; Chen, J. Recent Advances in Lead-Free Halide Perovskites for Photocatalysis. *ACS Mater. Lett.* **2022**, *5*, 60–78. [CrossRef]

13. Wang, J.; Shi, Y.; Wang, Y.; Li, Z. Rational design of metal halide perovskite nanocrystals for photocatalytic CO_2 reduction: Recent advances, challenges, and prospects. *ACS Energy Lett.* **2022**, *7*, 2043–2059. [CrossRef]

14. Zhu, Y.; Liu, Y.; Miller, K.A.; Zhu, H.; Egap, E. Lead halide perovskite nanocrystals as photocatalysts for PET-RAFT polymerization under visible and near-infrared irradiation. *ACS Macro Lett.* **2020**, *9*, 725–730. [CrossRef] [PubMed]

15. Zhu, Y.; Liu, Y.; Ai, Q.; Gao, G.; Yuan, L.; Fang, Q.; Lou, J. In situ synthesis of lead-free halide perovskite–COF nanocomposites as photocatalysts for photoinduced polymerization in both organic and aqueous phases. *ACS Mater. Lett.* **2022**, *4*, 464–471. [CrossRef]

16. Furasova, A.; Voroshilov, P.; Sapori, D.; Ladutenko, K.; Barettin, D.; Zakhidov, A.; Makarov, S. Nanophotonics for perovskite solar cells. *Adv. Photon. Res.* **2022**, *3*, 2100326. [CrossRef]

17. Chen, J.; Zhang, W.; Pullerits, T. Two-photon absorption in halide perovskites and their applications. *Mater. Horiz.* **2022**, *9*, 2255–2287. [CrossRef]

18. Skurlov, I.D.; Yin, W.; Ismagilov, A.O.; Tcypkin, A.N.; Hua, H.; Wang, H.; Zheng, W. Improved one-and multiple-photon excited photoluminescence from Cd^{2+}-doped $CsPbBr_3$ perovskite NCs. *Nanomaterials* **2022**, *12*, 151. [CrossRef] [PubMed]

19. Shen, W.; Chen, J.; Wu, J.; Li, X.; Zeng, H. Nonlinear optics in lead halide perovskites: Mechanisms and applications. *ACS Photon.* **2020**, *8*, 113–124. [CrossRef]

20. Sokolova, A.V.; Tepliakov, N.V.; Ismagilov, A.O.; Tatarinov, D.A.; Kalinichev, A.A.; Koroleva, A.V.; Litvin, A.P. Stoichiometry Control in Dual-Band Emitting Yb3+-Doped CsPbCl x Br3–x Perovskite Nanocrystals. *J. Phys. Chem. C* **2022**, *126*, 20550–20557. [CrossRef]

21. Wang, X.; Wang, Y.; Gao, W.; Song, L.; Ran, C.; Chen, Y.; Huang, W. Polarization-Sensitive Halide Perovskites for Polarized Luminescence and Detection: Recent Advances and Perspectives. *Adv. Mater.* **2021**, *33*, 2003615. [CrossRef]

22. Miao, J.; Zhang, F. Recent progress on highly sensitive perovskite photodetectors. *J. Mater. Chem. C* **2019**, *7*, 1741–1791. [CrossRef]

23. Mahapatra, A.S.; Kumar, P.; Kumar, P.; Pradhan, B. Recent progress in perovskite solar cells: Challenges from efficiency to stability. *Mater. Today Chem.* **2022**, *23*, 100686. [CrossRef]

24. Basumatary, P.; Pratima, A. A short review on progress in perovskite solar cells. *Mater. Res. Bull.* **2022**, *149*, 111700. [CrossRef]

25. Xia, C.; Peng, Q.; Poncé, J.; Patel, S.; Wright, J.B. Limits to electrical mobility in lead-halide perovskite semiconductors. *J. Phys. Chem. Lett.* **2021**, *12*, 3607–3617. [CrossRef] [PubMed]

26. Herz, L.M. Charge-carrier mobilities in metal halide perovskites: Fundamental mechanisms and limits. *ACS Energy Lett.* **2017**, *2*, 1539–1548. [CrossRef]

27. Liang, C.; Zhao, D.; Li, P.; Wu, B.; Gu, H.; Zhang, J. Simultaneously boost diffusion length and stability of perovskite for high performance solar cells. *Nano Energy* **2019**, *59*, 721–729. [CrossRef]

28. Yang, Z.; Yu, Z.; Wei, H.; Xiao, X.; Ni, Z.; Chen, B. Enhancing electron diffusion length in narrow-bandgap perovskites for efficient monolithic perovskite tandem solar cells. *Nat. Commun.* **2019**, *10*, 4498. [CrossRef] [PubMed]

29. Crespo, C.T. Absorption coefficients data of lead iodine perovskites using 14 different organic cations. *Data Brief* **2019**, *27*. [CrossRef]

30. Faridi, A.W.; Imran, M.; Tariq, G.H.; Ullah, S.; Noor, S.F.; Ansar, S.; Sher, F. Synthesis and characterization of high-efficiency halide perovskite nanomaterials for light-absorbing applications. *Ind. Eng. Chem. Res.* **2022**, *62*, 4494–4502. [CrossRef]

31. Hu, Z.; Lin, Z.; Su, J.; Zhang, J.; Chang, J.; Hao, Y. A review on energy band-gap engineering for perovskite photovoltaics. *Solar Rrl. Solar Rrl.* **2019**, *3*, 1900304. [CrossRef]

32. Tao, S.X.; Xi, C.; Bobbert, P.A. Accurate and efficient band gap predictions of metal halide perovskites using the DFT-1/2 method: GW accuracy with DFT expense. *Sci. Rep.* **2017**, *7*, 14386. [CrossRef] [PubMed]

33. Pachori, S.; Kumari, S.; Verma, A.S. An emerging high performance photovoltaic device with mechanical stability constants of hybrid ($HC(NH_2)_2PbI_3$) perovskite. *J. Mater. Sci. Mater. Electron.* **2020**, *31*, 18004–18017.

34. Targhi, F.F.; Jalili, Y.S.; Kanjouri, F. $MAPbI_3$ and $FAPbI_3$ perovskites as solar cells: Case study on structural, electrical and optical properties. *Res. Phys.* **2018**, *10*, 616–627. [CrossRef]

35. Cui, X.; Jin, J.; Tai, Q.; Yan, F. Recent Progress on the Phase Stabilization of FAPbI3 for High-Performance Perovskite Solar Cells. *Solar RRL.* **2022**, *6*, 2200497. [CrossRef]

36. Masi, S.; Gualdrón-Reyes, A.F.; Mora-Sero, I. Stabilization of black perovskite phase in FAPbI3 and CsPbI3. *ACS Energy Lett.* **2020**, *5*, 1974–1985. [CrossRef]

37. Liu, Y.; Akin, S.; Hinderhofer, A.; Eickemeyer, F.T.; Zhu, H.; Seo, J.Y. Stabilization of highly efficient and stable phase-pure FAPbI3 perovskite solar cells by molecularly tailored 2D-overlayers. *Angew. Chem. Int. Ed.* **2020**, *59*, 15688–15694. [CrossRef]

38. Chen, R.; Wu, Y.; Wang, Y.; Xu, R.; He, R.; Fan, Y. Crown Ether-Assisted Growth and Scaling Up of FACsPbI3 Films for Efficient and Stable Perovskite Solar Modules. *Adv. Funct. Mat.* **2021**, *31*, 2008760. [CrossRef]

39. Stranks, S.D.; Snaith, H.J. Metal-halide perovskites for photovoltaic and light-emitting devices. *Nat. Nanotechnol.* **2015**, *10*, 391–402. [CrossRef]

40. Min, H.; Kim, M.; Lee, S.U.; Kim, H.; Kim, G.; Choi, K.; Seok, S.I. Efficient, stable solar cells by using inherent bandgap of α-phase formamidinium lead iodide. *Science* **2019**, *366*, 749–753. [CrossRef]

41. Yang, D.; Yang, R.; Wang, K.; Wu, C.; Zhu, X.; Feng, J.; Liu, S. High efficiency planar-type perovskite solar cells with negligible hysteresis using EDTA-complexed SnO_2. *Nat. Commun.* **2018**, *9*, 3239. [CrossRef]

42. Yang, L.; Zhou, H.; Duan, Y.; Wu, M.; He, K.; Li, Y. 24.96%-Efficiency FACsPbI3 Perovskite Solar Cells Enabled by Intermolecular Esterification Reaction of DL-Carnitine Hydrochloride. *Adv. Mat.* **2023**, *25*, 2211545. [CrossRef]

43. Thote, A.; Jeon, I.; Lee, J.W.; Seo, S.; Lin, H.S.; Yang, Y. Stable and reproducible 2D/3D formamidinium–lead–iodide perovskite solar cells. *ACS Appl. Energy Mater.* **2019**, *2*, 2486–2493. [CrossRef]

44. Liu, J.; Rui, L.; Bai, Y. Carbon dots: A new type of carbon-based nanomaterial with wide applications. *ACS Central Sci.* **2020**, *6*, 2179–2195. [CrossRef] [PubMed]

45. Cui, L.; Ren, X.; Sun, M.; Liu, H.; Xia, L. Carbon dots: Synthesis, properties, and applications. *Nanomaterials.* **2021**, *11*, 3419. [CrossRef] [PubMed]

46. Litvin, A.P.; Zhang, X.; Berwick, K.; Fedorov, A.V.; Zheng, W.; Baranov, A.V. Carbon-based interlayers in perovskite solar cells. *Renew. Sustain. Energy Rev.* **2020**, *124*, 109774. [CrossRef]

47. Litvin, A.P.; Zhang, X.; Ushakova, E.V.; Rogach, A.L. Carbon Nanoparticles as Versatile Auxiliary Components of Perovskite-Based Optoelectronic Devices. *Adv. Funct. Mater.* **2021**, *31*, 2010768. [CrossRef]

48. Stepanidenko, E.A.; Ushakova, E.V.; Fedorov, A.V.; Rogach, A.L. Applications of carbon dots in optoelectronics. *Nanomaterials* **2021**, *11*, 364. [CrossRef]

49. Yadeta, T.F.; Huang, K.W.; Imae, T.; Tung, Y.L. Enhancement of Perovskite Solar Cells by TiO_2-Carbon Dot Electron Transport Film Layers. *Nanomaterials* **2022**, *13*, 186. [CrossRef]

50. Alkahtani, M.; Alenzi, S.M.; Alsolami, A.; Alsofyani, N.; Alfahd, A.; Alzahrani, Y.A.; Abduljawad, M. High-Performance and Stable Perovskite Solar Cells Using Carbon Quantum Dots and Upconversion Nanoparticles. *Int. J. Mol. Sci.* **2022**, *23*, 14441. [CrossRef]

51. Zhang, X.; Zeng, Q.; Xiong, Y.; Ji, T.; Wang, C.; Shen, X.; Zheng, W. Energy level modification with carbon dot interlayers enables efficient perovskite solar cells and quantum dot based light-emitting diodes. *Adv. Funct. Mater.* **2020**, *30*, 1910530. [CrossRef]

52. Ma, Y.; Zhang, H.; Zhang, Y.; Hu, R.; Jiang, M.; Zhang, R. Enhancing the performance of inverted perovskite solar cells via grain boundary passivation with carbon quantum dots. *ACS Appl. Mat. Interf.* **2018**, *11*, 3044–3052. [CrossRef]

53. Ma, Y.; Zhang, H.; Zhang, Y.; Hu, R.; Jiang, M.; Zhang, R. Surface passivation with nitrogen-doped carbon dots for improved perovskite solar cell performance. *J. Mater. Sci.* **2018**, *53*, 9180–9190.

54. Fang, X.; Ding, J.; Yuan, N.; Sun, P.; Lv, M.; Ding, G.; Zhu, C. Graphene quantum dot incorporated perovskite films: Passivating grain boundaries and facilitating electron extraction. *Phys. Chem. Chem. Phys.* **2017**, *19*, 6057–6063. [CrossRef] [PubMed]

55. Wen, Y.; Zhu, G.; Shao, Y. Improving the power conversion efficiency of perovskite solar cells by adding carbon quantum dots. *J. Mater. Sci.* **2020**, *55*, 2937–2946. [CrossRef]

56. Sánchez-Godoy, H.E.; Erazo, E.A.; Gualdrón-Reyes, A.F.; Khan, A.H.; Agouram, S.; Barea, E.M.; Mora-Seró, I. Preferred growth direction by PbS nanoplatelets preserves perovskite infrared light harvesting for stable, reproducible, and efficient solar cells. *Adv. Energy Mater.* **2020**, *10*, 2002422. [CrossRef]

57. Parfenov, P.S.; Litvin, A.P.; Ushakova, E.V.; Fedorov, A.V.; Baranov, A.V.; Berwick, K. Note: Near infrared spectral and transient measurements of PbS quantum dots luminescence. *Rev. Sci. Instrum.* **2013**, *84*, 116104. [CrossRef] [PubMed]

58. Xiang, Z.; Jiang, Y.; Cui, C.; Luo, Y.; Peng, Z. Sensitive, Selective and Reliable Detection of Fe^{3+} in Lake Water via Carbon Dots-Based Fluorescence Assay. *Molecules* **2022**, *27*, 6749. [CrossRef]

59. Wang, B.; Wei, Z.; Sui, L.; Yu, J.; Zhang, B.; Wang, X.; Lu, S. Electron–phonon coupling-assisted universal red luminescence of o-phenylenediamine-based carbon dots. *Light Sci. Appl.* **2022**, *11*, 172. [CrossRef]

60. Channa, A.M.; Siyal, A.N.; Memon, S.Q.; Parveen, S. Design of experiment for treatment of arsenic-contaminated water using Schiff's base metal complex modified Amberlite XAD-2. *Desalin. Water Treat.* **2016**, *57*, 3664–3673. [CrossRef]

61. Dong, W.; Zhang, X.; Yang, F.; Zeng, Q.; Yin, W.; Zhang, W.; Zheng, W. Amine-terminated carbon dots linking hole transport layer and vertically oriented quasi-2D perovskites through hydrogen bonds enable efficient LEDs. *ACS Nano* **2022**, *16*, 9679–9690. [CrossRef]

62. Liu, B.T.; Zhang, Y.Z.; Zuo, Y.Y.; Rachmawati, D. Passivation and energy-level change of the SnO_2 electron transport layer by reactive titania for perovskite solar cells. *J. Alloys Compd.* **2022**, *929*, 167349. [CrossRef]

63. Huang, S.K.; Wang, Y.C.; Ke, W.C.; Kao, Y.T.; She, N.Z.; Li, J.X.; Chen, C.W. Unravelling the origin of the photocarrier dynamics of fullerene-derivative passivation of SnO_2 electron transporters in perovskite solar cells. *J. Mater. Chem. A* **2020**, *8*, 23607–23616. [CrossRef]

64. Zhu, Z.; Ma, J.; Wang, Z.; Mu, C.; Fan, Z.; Du, L.; Yang, S. Efficiency enhancement of perovskite solar cells through fast electron extraction: The role of graphene quantum dots. *J. Am. Chem. Soc.* **2014**, *136*, 3760–3763. [CrossRef] [PubMed]

65. Kulbak, M.; Gupta, S.; Kedem, N.; Levine, I.; Bendikov, T.; Hodes, G.; Cahen, D. Cesium enhances long-term stability of lead bromide perovskite-based solar cells. *J. Phys. Chem. Lett.* **2016**, *7*, 167–172. [CrossRef]

66. Benetti, D.; Jokar, E.; Yu, C.H.; Fathi, A.; Zhao, H.; Vomiero, A.; Rosei, F. Hole-extraction and photostability enhancement in highly efficient inverted perovskite solar cells through carbon dot-based hybrid material. *Nano Energy* **2019**, *62*, 781–790. [CrossRef]

67. Gan, X.; Yang, S.; Zhang, J.; Wang, G.; He, P.; Sun, H.; Zhu, Y. Graphite-N doped graphene quantum dots as semiconductor additive in perovskite solar cells. *ACS Appl. Mater. Interf.* **2019**, *11*, 37796–37803. [CrossRef]
68. Kirbiyik, C.; Toprak, A.; Baslak, C.; Kus, M.; Ersoz, M. Nitrogen-doped CQDs to enhance the power conversion efficiency of perovskite solar cells via surface passivation. *J. Alloys Compd.* **2020**, *832*, 154897. [CrossRef]
69. Yeh, T.F.; Teng, C.Y.; Chen, S.J.; Teng, H. Nitrogen-doped graphene oxide quantum dots as photocatalysts for overall water-splitting under visible light Illumination. *Adv. Mater.* **2014**, *26*, 3297–3303. [CrossRef]